Journal of Alloys and Compounds 516 (2012) 144–152

Contents lists available at SciVerse ScienceDirect

Journal of Alloys and Compounds

journal homepage: www.elsevier.com/locate/jallcom

Effects of annealing on $Zr_8Ni_{19}X_2$ (X = Ni, Mg, Al, Sc, V, Mn, Co, Sn, La, and Hf): Structural characteristics

J. Nei [a], K. Young [b,*], S.O. Salley [a], K.Y.S. Ng [a]

[a] *Department of Chemical Engineering, Wayne State University, Detroit, MI 48202, USA*
[b] *Energy Conversion Devices Inc./Ovonic Battery Company, 2983 Waterview Drive, Rochester Hills, MI 48309, USA*

ARTICLE INFO

Article history:
Received 27 September 2011
Received in revised form
28 November 2011
Accepted 29 November 2011
Available online 9 December 2011

Keywords:
Hydrogen absorbing materials
Transition metal alloys
Zr—Ni alloy

ABSTRACT

The effects of an 8-h annealing treatment at 960 °C on the phase structures of a series of partial-Ni substituted Zr_8Ni_{21} alloys, potential metal hydride candidates for high-rate nickel/metal hydride batteries, were studied. The substitution elements included Mg, Al, Sc, V, Mn, Co, Sn, La, and Hf. Only the main phase of the annealed Sn-substitution remained Zr_8Ni_{21}-structured while those of other substitutions turned into Zr_7Ni_{10} or Zr_2Ni_7. Similar to the preference of C14/C15 main phase in AB_2 alloys, the number of outer-shell electrons played an important role in determining the main phase of the A_8B_{21} alloys. As the number of outer-shell electrons of the substituting element increased, the main phase evolved from tetragonal Zr_7Ni_{10} (Mg, Al, and Sc), to orthorhombic Zr_7Ni_{10} (La and Hf), cubic Zr_2Ni_7 (V, Mn, Co, and Sn (before annealing)), and finally triclinic Zr_8Ni_{21} (Ni and Sn (after annealing)). After annealing, the abundance of the predominant phase increased, and the number of secondary phases diminished. The only exception was the Sn-substituted alloy, where the major phase transformed from Zr_2Ni_7 to Zr_8Ni_{21} (after annealing). In this study, several alloys showed an X-ray diffraction peak at around 38.4°, which cannot be correlated to any phase in the database. The stoichiometry of this phase is close to Zr_2Ni_7 according to X-ray energy dispersive spectroscopy.

© 2011 Elsevier B.V. All rights reserved.

1. Introduction

Zr, Ti-based AB_2 metal hydride (MH) alloy is considered to be one of the most promising candidates to replace the misch metal-based AB_5 alloys presently used as the negative electrode in nickel/metal hydride (Ni/MH) batteries, especially for the purpose of reducing the industry's dependence on rare earth elements imported from China [1,2]. Since most of the studies on AB_2 MH alloys focus on multi-element and highly disordered families [3], the understanding of basic Ti—Ni and Zr—Ni inter-metallic alloys is crucial for fully utilizing the synergetic effects between the main AB_2 Laves phases and the non-Laves secondary phases [4,5].

The stoichiometry of AB_2 was chosen for the transition-metal based MH alloys by considering the balance between large storage capacity (lower hydride heat of formation) and high discharge capability (higher hydride heat of formation) [3,6,7]. However, there is no AB_2 inter-metallic alloy for either Zr—Ni or Ti—Ni binary systems. In Fig. 1 [8], the Zr—Ni binary phase diagram shows eight inter-metallic alloys: $ZrNi_5$, Zr_2Ni_7, $ZrNi_3$, Zr_8Ni_{21}, Zr_7Ni_{10}, Zr_9Ni_{11}, ZrNi, and Zr_2Ni, of which the closest inter-metallic compounds to AB_2 are Zr_7Ni_{10} and Zr_8Ni_{21}. Compared to AB_2 alloys, the former alloy, Zr_7Ni_{10}, has a slightly stronger metal—hydrogen bond strength due to its higher A to B ratio (0.70) and solidifies congruently from liquid. It should be noted that this version of the Zr—Ni binary phase diagram was recently proposed by Okamoto [8] and shows a very narrow solubility range of the Zr_7Ni_{10} phase. This differs from the conventional phase diagram that shows a broad composition range for the Zr_7Ni_{10} phase [9]. In a practical MH alloy, Zr was replaced partially by Ti to reduce the metal—hydrogen bond strength [10]. Other substituting elements have also been studied in order to improve the electrochemical properties [11–13]. The latter alloy, Zr_8Ni_{21}, was chosen as the focus of this report. Contrary to the property of Zr_7Ni_{10}, Zr_8Ni_{21} has a slightly weaker metal—hydrogen bond due to its higher concentration of B; therefore, adjusting B by partially replacing Ni with other elements is applied in this study to potentially increase the metal—hydrogen bond strength. Furthermore, Zr_8Ni_{21} does not solidify directly from the liquid as in the case of Zr_7Ni_{10}. Instead, Zr_2Ni_7 is first solidified from the liquid with a Zr-to-Ni ratio of 8:21 and later reacts with the remaining liquid to form Zr_8Ni_{21} alloy peritectically [14]. If the condition of equilibrium is not reached during cooling, one or more secondary phases will precipitate out. Therefore, an annealing process was adopted for this study. The crystal structure of Zr_8Ni_{21} is triclinic [15], which is isotropic to that of Hf_8Ni_{21} [16]. The lattice parameters are $a = 6.476$ Å, $b = 8.064$ Å, $c = 8.594$ Å, $\alpha = 75.15°$, $\beta = 68.07°$, and $\gamma = 75.23°$ as determined by X-ray diffraction (XRD) analysis.

---

* Corresponding author. Tel.: +1 248 293 7000; fax: +1 248 299 4520.
E-mail address: kwoyoung@yahoo.com (K. Young).

0925-8388/$ – see front matter © 2011 Elsevier B.V. All rights reserved.
doi:10.1016/j.jallcom.2011.11.153

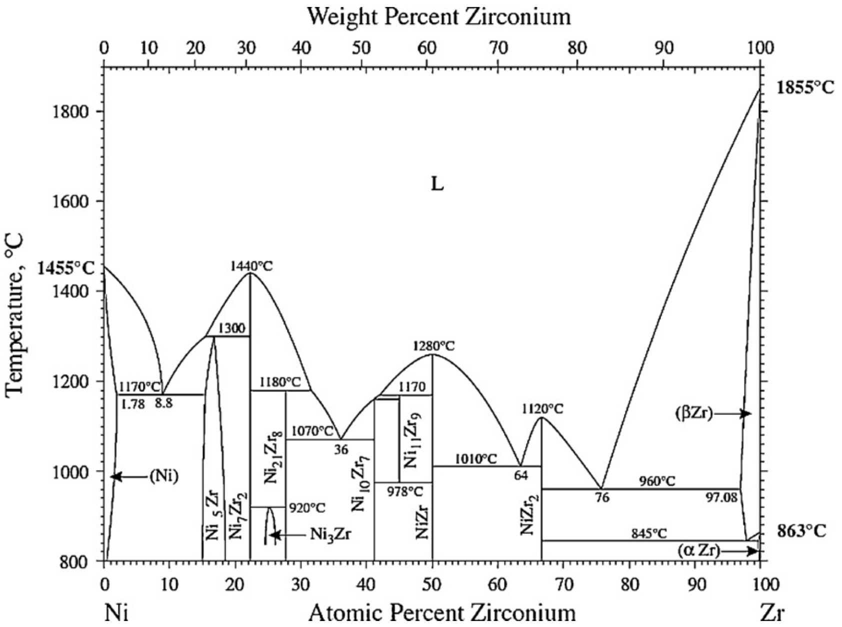

Fig. 1. Zr—Ni binary phase diagram showing a very narrow solubility range of Zr_7Ni_{10} phase [8].

The coordination number of Zr in this structure is 15 and that from other 11 non-equivalent Ni varies between 12 and 13. The XRD pattern reported by Ruiz et al. on a Zr_8Ni_{21} sample annealed at 1000 °C for 30 days includes an additional broad peak between 37.5° and 39.5° besides those identified as reflections from the Zr_8Ni_{21} structure when compared to Hf_8Ni_{21} [17]. This extra broad peak is believed to belong to a microcrystalline ZrNi phase according to the current study and will be discussed in later sections. Although the properties of un-modified Zr_8Ni_{21} were reported in the past, a systematic study of the effects from compositional modification and annealing on Zr_8Ni_{21} has not been performed in the past and will be presented in the current study, focusing on the phase constituents before and after the annealing treatment.

2. Experimental setup

Samples were prepared by arc melting under a continuous argon flow with a non-consumable tungsten electrode and a water-cooled copper tray. Before each arc melt, a piece of sacrificial titanium underwent a few melting-cooling cycles to reduce the residual oxygen concentration in the system. Each 10-g sample ingot was re-melted and flipped over a few times to ensure uniformity in chemical composition. Half of each sample was annealed at 960 °C for 8 h in an argon environment. The chemical composition of each sample was examined with a Varian *Liberty* 100 inductively coupled plasma (ICP) system. A Rigaku *Miniflex* XRD was used to study each alloy's microstructure. A JOEL *JSM6320F* Scanning Electron Microscope (SEM) with X-ray energy dispersive spectroscopy (EDS) capability was used to study the phase distribution and composition. Samples for SEM/EDS analysis were mounted and polished on epoxy blocks, rinsed and dried before entering the SEM chamber.

3. Results and discussion

10 alloys, Zr_8Ni_{21} (ZN-Ni), $Zr_8Ni_{19}Mg_2$ (ZN-Mg), $Zr_8Ni_{19}Al_2$ (ZN-Al), $Zr_8Ni_{19}Sc_2$ (ZN-Sc), $Zr_8Ni_{19}V_2$ (ZN-V), $Zr_8Ni_{19}Mn_2$ (ZN-Mn), $Zr_8Ni_{19}Co_2$ (ZN-Co), $Zr_8Ni_{19}Sn_2$ (ZN-Sn), $Zr_8Ni_{19}La_2$ (ZN-La), and $Zr_8Ni_{19}Hf_2$ (ZN-Hf), were prepared with raw materials from 99.999% purity metals except for ZN-Mg, where a $MgNi_2$ mother ingot was the source of Mg due to Mg's low boiling point. ICP analysis showed the compositions of these alloys to be very close to their designed values. The annealed samples were designated as samples ZN-*X*A, where *X* is the substituting element in the formula $Zr_8Ni_{19}X_2$. An annealing temperature of 960 °C was chosen to prevent liquid from forming during annealing. The sample ZN-MgA had very little Mg-content after the annealing process and therefore was removed from the experiment matrix of this study.

Al, Mn, and Co are frequently used to modify the electrochemical properties of AB_5, A_2B_7, and AB_2 MH alloys [18–27]. Sn has been added to AB_2 MH alloys for performance studies due to the potential to reduce raw material cost [28]. V is commonly used as a modifier in AB_2 MH alloys [29,30]. Mg, Sc, La, and Hf were chosen with the intention to enlarge the unit cell and increase the hydrogen storage capacity. A few important properties of the modifying elements, such as atomic number, electronegativity, metallic radius, number of outer-shell electrons, and oxidation potential are listed in Table 1. The phase transformations during cooling for target compositions of Zr_8X_{21} and X_2Ni_{19}, where *X* is the one of the ten substituting elements, are summarized in Table 2. The solidification processes of Zr_8X_{21} are very different, from immiscible (Mg, La) to eutectic (Al, Mn, Sn), eutectoid (V), peritectic (Ni), to solid solution (Sc, Co, Hf). The XRD patterns of the 19 samples (10 before annealing and 9 after annealing) are displayed in Fig. 2. All peaks, except for the one near 38.4°, are identified and indexed according to the Powder Diffraction File database [31]. With the help of Jade 9 software, the lattice

Table 1
Basic properties of all elements used in this study. Electronegativity of an element represents the affinity to additional electron. Metallic radius is from 12-coordinated metal. Oxidation potential is measured between the metal and the lowest oxidation state.

	Zr	Ni	Mg	Al	Sc	V	Mn	Co	Sn	La	Hf
Atomic number	40	28	12	13	21	23	25	27	50	57	72
Electronegativity [44]	1.33	1.91	1.31	1.61	1.36	1.63	1.55	1.88	1.96	1.10	1.30
Metallic radius (Å) [45]	1.60	1.25	1.60	1.43	1.64	1.35	1.26	1.25	1.55	1.88	1.58
Number of outer-shell electrons	4	10	2	3	3	5	7	9	14	3	4
Oxidation potential (volt vs. SHE) [46]	−1.45	−0.257	−2.70	−1.662	−2.077	−1.175	−1.185	−0.28	−0.138	−2.379	−1.55

Table 2
The phase transformations during cooling for target compositions of Zr_8X_{21} and X_2Ni_{19} [9].

	Zr_8X_{21} (Zr = 27.6 at.%)	X_2Ni_{19} (X = 9.5 at.%)
X = Ni	Peritectic @ 1180 °C	Congruent
X = Mg	Immiscible	Eutectic @ 1097 °C ($MgNi_2$ + Ni)
X = Al	Eutectic @ 1490 °C ($ZrAl_2$ + $ZrAl_3$)	Eutectic @ 1385 °C ($AlNi_3$ + Ni)
X = Sc	Solid solution	Eutectic @ 1140 °C ($ScNi_5$ + Ni)
X = V	Eutectoid @ 1300 °C (V + C15-ZrV_2)	Congruent @ 405 °C
X = Mn	Eutectic @ 1160 °C (Mn + C14-$ZrMn_2$)	Solid solution
X = Co	Solid solution	Solid solution
X = Sn	Eutectic @ 232 °C (Sn + C54-$ZnSn_2$)	Eutectoid @ 920.5 °C ($SnNi_3$ + Ni)
X = La	Immiscible	Eutectic @ 1270 °C ($LaNi_5$ + Ni)
X = Hf	Solid solution	Eutectic @ 1190 °C ($HfNi_5$ + Ni)

constants and unit cell volumes of major phases in each sample were calculated based on its XRD pattern and are listed in Table 3 together with the reference data. Notably, the lattice constants of some phases could not be calculated due to insufficient number of peaks and are therefore not shown in Table 3. The microstructures of the 19 samples were studied using SEM, with which both the secondary electron images (BEI) and the back-scattering electron images (BEI) were taken. 10 BEI micrographs were chosen to represent each of the important main and secondary phases and are presented in Fig. 3 with the same magnification. With the help of surface morphology analysis (done by examining the SEI micrographs), the compositions in several areas (identified numerically in the micrographs) were studied using EDS and the results are listed in Table 4. Combining the XRD and SEM/EDS results, the phase analyses of all samples, before and after annealing, are presented in the following sections.

3.1. Zr_8Ni_{21} base alloy

The XRD pattern of ZN-Ni is composed of mainly Zr_8Ni_{21} peaks (Fig. 2a). Besides the reflections from Zr_8Ni_{21}, there is one extra broad peak at around 38.5°. In the study of AB_2 and A_7B_{10} alloys, similar broad peaks were found and assigned to orthorhombic ZrNi phase [11,32]. A peak at the same angle had also been recorded in the XRD pattern of Zr_8Ni_{21} reported previously [17]. The unit cell of Zr_8Ni_{21} is smaller than that listed in the database (Table 3). Due to the formation of ZrNi, the Zr-to-Ni ratio in Zr_8Ni_{21} phase

Table 3
The lattice constants of major phases in each sample and their corresponding reference data [31]. a, b, and c are in Å, α, β, and γ are in degrees, and volumes are in $Å^3$.

	Phase	Structure	PDF file #	Reference data	Reference volume	Measured data	Measured volume
ZN-Ni	Zr_8Ni_{21}	Triclinic	04-002-9932	$(a, b, c) = (6.4721, 8.0645, 8.5878)$ $(\alpha, \beta, \gamma) = (75.19, 68.04, 75.26)$	395.54	(6.479, 8.045, 8.522) (75.30, 67.87, 75.15)	391.55
ZN-NiA	Zr_8Ni_{21}	Triclinic	04-002-9932	$(a, b, c) = (6.4721, 8.0645, 8.5878)$ $(\alpha, \beta, \gamma) = (75.19, 68.04, 75.26)$	395.54	(6.497, 8.021, 8.515) (75.34, 67.88, 75.33)	391.47
ZN-Mg	Zr_7Ni_{10}	Tetragonal	00-056-1231	$(a, b, c) = (6.4956, 6.4956, 12.3610)$	521.55	(6.487, 6.487, 12.338)	519.20
	Zr_2Ni_7	Cubic	00-037-0925	$(a, b, c) = (6.68, 6.68, 6.68)$	298.08	(6.90, 6.90, 6.90)	328.51
ZN-Al	Zr_7Ni_{10}	Tetragonal	00-056-1231	$(a, b, c) = (6.4956, 6.4956, 12.3610)$	521.55	(6.488, 6.488, 12.271)	516.54
	Zr_2Ni_7	Cubic	00-037-0925	$(a, b, c) = (6.68, 6.68, 6.68)$	298.08	(6.93, 6.93, 6.93)	332.81
ZN-AlA	Zr_7Ni_{10}	Tetragonal	00-056-1231	$(a, b, c) = (6.4956, 6.4956, 12.3610)$	521.55	(6.495, 6.495, 12.254)	516.94
	Zr_2Ni_7	Cubic	00-037-0925	$(a, b, c) = (6.68, 6.68, 6.68)$	298.08	(6.93, 6.93, 6.93)	332.81
ZN-Sc	Zr_7Ni_{10}	Tetragonal	00-056-1231	$(a, b, c) = (6.4956, 6.4956, 12.3610)$	521.55	(6.483, 6.483, 12.313)	517.51
	Zr_2Ni_7	Cubic	00-037-0925	$(a, b, c) = (6.68, 6.68, 6.68)$	298.08	(6.91, 6.91, 6.91)	329.94
ZN-ScA	Zr_7Ni_{10}	Tetragonal	00-056-1231	$(a, b, c) = (6.4956, 6.4956, 12.3610)$	521.55	(6.483, 6.483, 12.313)	517.51
	Zr_2Ni_7	Cubic	00-037-0925	$(a, b, c) = (6.68, 6.68, 6.68)$	298.08	(6.91, 6.91, 6.91)	329.94
ZN-V	Zr_7Ni_{10}	Tetragonal	00-056-1231	$(a, b, c) = (6.4956, 6.4956, 12.3610)$	521.55	(6.421, 6.421, 12.190)	502.58
	Zr_2Ni_7	Cubic	00-037-0925	$(a, b, c) = (6.68, 6.68, 6.68)$	298.08	(6.89, 6.89, 6.89)	327.08
ZN-VA	Zr_2Ni_7	Cubic	00-037-0925	$(a, b, c) = (6.68, 6.68, 6.68)$	298.08	(6.90, 6.90, 6.90)	328.51
ZN-Mn	Zr_7Ni_{10}	Tetragonal	00-056-1231	$(a, b, c) = (6.4956, 6.4956, 12.3610)$	521.55	(6.498, 6.498, 12.302)	519.44
	Zr_2Ni_7	Cubic	00-037-0925	$(a, b, c) = (6.68, 6.68, 6.68)$	298.08	(6.91, 6.91, 6.91)	329.94
ZN-MnA	Zr_2Ni_7	Cubic	00-037-0925	$(a, b, c) = (6.68, 6.68, 6.68)$	298.08	(6.92, 6.92, 6.92)	331.37
ZN-Co	Zr_7Ni_{10}	Tetragonal	00-056-1231	$(a, b, c) = (6.4956, 6.4956, 12.3610)$	521.55	(6.491, 6.491, 12.320)	519.08
	Zr_2Ni_7	Cubic	00-037-0925	$(a, b, c) = (6.68, 6.68, 6.68)$	298.08	(6.90, 6.90, 6.90)	328.51
	$ZrNi_5$	Cubic	00-037-0924	$(a, b, c) = (6.68, 6.68, 6.68)$	298.08	(6.71, 6.71, 6.71)	302.11
ZN-CoA	Zr_2Ni_7	Cubic	00-037-0925	$(a, b, c) = (6.68, 6.68, 6.68)$	298.08	(6.89, 6.89, 6.89)	327.08
ZN-Sn	Zr_2Ni_7	Cubic	00-037-0925	$(a, b, c) = (6.68, 6.68, 6.68)$	298.08	(6.91, 6.91, 6.91)	329.94
	$ZrNi_5$	Cubic	00-037-0924	$(a, b, c) = (6.68, 6.68, 6.68)$	298.08	(6.61, 6.61, 6.61)	288.80
	Zr_2SnNi_2	Tetragonal	00-048-1703	$(a, b, c) = (7.0659, 7.0659, 3.4145)$	170.48	(7.054, 7.054, 3.406)	169.48
	$ZrSnNi_2$	Cubic	00-023-1282	$(a, b, c) = (6.27, 6.27, 6.27)$	246.49	(6.25, 6.25, 6.25)	244.14
ZN-SnA	Zr_2SnNi_2	Tetragonal	00-048-1703	$(a, b, c) = (7.0659, 7.0659, 3.4145)$	170.48	(7.085, 7.084, 3.390)	170.12
	$ZrSnNi_2$	Cubic	00-023-1282	$(a, b, c) = (6.27, 6.27, 6.27)$	246.49	(6.28, 6.28, 6.28)	248.01
ZN-La	Zr_7Ni_{10}	Orthorhombic	00-047-1027	$(a, b, c) = (12.385, 9.154, 9.216)$	1044.84	(12.436, 9.166, 9.162)	1044.36
	Zr_8Ni_{21}	Triclinic	004-002-9932	$(a, b, c) = (6.4721, 8.0645, 8.5878)$ $(\alpha, \beta, \gamma) = (75.19, 68.04, 75.26)$	395.54	(6.430, 8.033, 8.645) (75.33, 68.03, 75.39)	394.39
	LaNi	Orthorhombic	00-019-0654	$(a, b, c) = (3.907, 10.810, 4.396)$	185.66	(3.910, 10.810, 4.385)	185.34
	$LaNi_5$	Hexagonal	00-055-0277	$(a, b, c) = (5.0167, 5.0167, 3.9783)$	260.13	(5.019, 5.019, 4.054)	265.32
ZN-LaA	Zr_7Ni_{10}	Orthorhombic	00-047-1027	$(a, b, c) = (12.385, 9.154, 9.216)$	1044.84	(12.301, 9.199, 9.175)	1038.21
	Zr_2Ni_7	Cubic	00-037-0925	$(a, b, c) = (6.68, 6.68, 6.68)$	298.08	(6.92, 6.92, 6.92)	331.37
	LaNi	Orthorhombic	00-019-0654	$(a, b, c) = (3.907, 10.810, 4.396)$	185.66	(3.904, 10.797, 4.389)	185.00
	$LaNi_5$	Hexagonal	00-055-0277	$(a, b, c) = (5.0167, 5.0167, 3.9783)$	260.13	(5.065, 5.065, 4.005)	270.27
ZN-Hf	Zr_7Ni_{10}	Orthorhombic	00-047-1027	$(a, b, c) = (12.385, 9.154, 9.216)$	1044.84	(12.384, 9.190, 9.130)	1039.08
	Zr_8Ni_{21}	Triclinic	04-002-9932	$(a, b, c) = (6.4721, 8.0645, 8.5878)$ $(\alpha, \beta, \gamma) = (75.19, 68.04, 75.26)$	395.54	(6.451, 8.047, 8.531) (75.12, 67.94, 75.15)	390.30
ZN-HfA	Zr_7Ni_{10}	Orthorhombic	00-047-1027	$(a, b, c) = (12.385, 9.154, 9.216)$	1044.84	(12.317, 9.151, 9.141)	1030.31
	Zr_8Ni_{21}	Triclinic	04-002-9932	$(a, b, c) = (6.4721, 8.0645, 8.5878)$ $(\alpha, \beta, \gamma) = (75.19, 68.04, 75.26)$	395.54	(6.493, 8.004, 8.504) (75.67, 67.75, 75.54)	390.28

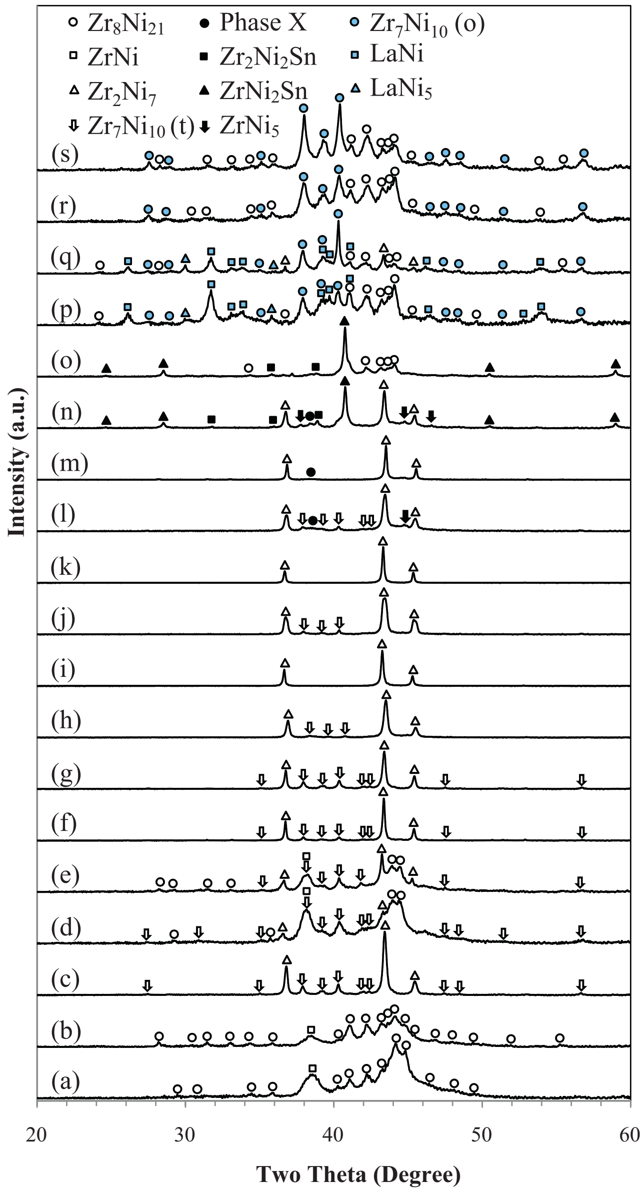

Fig. 2. XRD patterns using Cu-K$_\alpha$ as the radiation source for ZN-Ni (a), ZN-NiA (b), ZN-Mg (c), ZN-Al (d), ZN-AlA (e), ZN-Sc (f), ZN-ScA (g), ZN-V (h), ZN-VA (i), ZN-Mn (j), ZN-MnA (k), ZN-Co (l), ZN-CoA (m), ZN-Sn (n), ZN-SnA (o), ZN-La (p), ZN-LaA (q), ZN-Hf (r), and ZN-HfA (s) samples.

is decreased. This hyper-stoichiometry may have caused anti-site defect (partial replacement of Zr by Ni in the A-site) or vacancy defect (vacant A-site as a result of insufficient amount of Zr) in the structure and consequently reduces the unit cell volume. Since the peak of ZrNi is broad, which corresponds to very fine crystallites, individual ZrNi grains are too fine to be seen in the SEM micrograph (Fig. 3a). Instead, ZrNi grains are distributed throughout the Zr_8Ni_{21} matrix and form area 1. Although $ZrNi_5$ is not detected by XRD, area 3 is suspected to be a mixture of Zr_8Ni_{21} and $ZrNi_5$ due to its (Ni + X)/Zr ratio and the discovery of $ZrNi_5$ existence in the annealed sample discussed later in this section.

After annealing, the Zr_8Ni_{21} phase predominates the microstructure, and the broad peak at around 38.5° is still present (Fig. 2b) with an intensity lower than the one prior to annealing while the intensities of other peaks increase after annealing. Since annealing decreases the amount of secondary phases, the XRD results before and after annealing further show that the broad peak at around 38.5° does not belong to Zr_8Ni_{21} family and should be ZrNi. The unit cell volume of Zr_8Ni_{21} is similar to that from the unannealed sample. From the SEM micrograph (Fig. 3b), fine grains of ZrNi are mixed throughout the Zr_8Ni_{21} matrix and increase the Zr-contents in areas 1 and 2. Occasionally, dagger-shaped $ZrNi_5$ grains are found in the SEM micrograph (area 4), but the amount is too small to be detected by XRD. This observation also shows that despite not being seen in the micrograph, $ZrNi_5$ exists as fine crystallite in the unannealed alloy. The annealing process promotes the accumulation of the fine $ZrNi_5$ grains, which is evident in the SEM micrograph.

3.2. $Zr_8Ni_{19}Mg_2$ alloy

Mg is much larger and lighter than Ni with large differences in both electronegativity and number of outer-shell electrons. The XRD pattern of ZN-Mg shows a peak profile composed of tetragonal Zr_7Ni_{10} phase (Zr_7Ni_{10} (t)) and a face-center-cubic-structured (FCC) phase, which is designated as Zr_2Ni_7 on the basis of the EDS result and understanding of possible phase formation discussed later in this section (Fig. 2c). Zr_7Ni_{10} is an important secondary phase formed by a solid transformation from B2 during the solidification of common AB_2 MH alloys [33]. Two structures are available for Zr_7Ni_{10} stoichiometry: the as-prepared Zr_7Ni_{10}, which usually shows an orthorhombic structure, and the material after hydride/dehydride cycle or prepared by quenching, which exhibits a tetragonal structure [34,35]. While the unit cell of Zr_7Ni_{10} (t) is slightly smaller than the one calculated based on the database, the unit cell of Zr_2Ni_7 is 10% larger than the stoichiometric Zr_2Ni_7 crystal.

The SEM micrograph shows a Zr_7Ni_{10} matrix with granular Zr_2Ni_7 and occasional Mg_2Ni inclusions. The solubility of Mg in the Zr_7Ni_{10} matrix is not detectable by EDS due to the immiscible nature of Mg and Zr (Table 2). The (Ni + X)/Zr ratio in Zr_7Ni_{10} phase is higher than the stoichiometric value (1.43), which can be used to explain its slightly smaller unit cell when compared to that listed in the database. This hyper-stoichiometry indicates a composition range of the Zr_7Ni_{10} phase, which is closer to the original phase diagram proposed by Massalski [9]. It is suspected that the raw materials used in Massalski's version of the phase diagram are not 100% pure, which is similar to this study where additional modifiers are added into the formula, so the composition range of Zr_7Ni_{10} widens from the narrow line suggested by Okamoto [8] (Fig. 1). Regarding the peaks from a FCC structure, in the Zr—Ni system, an AB_2 (C15) FCC structure is not available. Both Zr_2Ni_7 and $ZrNi_5$ have similar reflection patterns in the same neighborhood. Considering the (Ni + X)/Zr ratio, this FCC-structured phase is assigned to Zr_2Ni_7. However, this ratio is much lower than the stoichiometry of Zr_2Ni_7 (3.50). In contrast with the effect of hyper-stoichiometry discussed previously, this hypo-stoichiometry increases the unit cell volume of the Zr_2Ni_7 phase.

3.3. $Zr_8Ni_{19}Al_2$ alloy

Al is another light element used in this study. Similar to the case of Mg, Al is larger than Ni with smaller differences in electronegativity and number of outer-shell electrons. The XRD pattern from unannealed ZN-Al shows a mixture of Zr_7Ni_{10} (t), Zr_2Ni_7, Zr_8Ni_{21}, and ZrNi phases (Fig. 2d). Due to the hyper-stoichiometry in Zr_7Ni_{10} (t) (Table 4), which is similar to the case in ZN-Mg, the unit cell of Zr_7Ni_{10} (t) in ZN-Al is smaller than that listed in the database. The unit cell of Zr_2Ni_7 in ZN-Al is the largest among all the Zr_2Ni_7 phases observed in this study (all are higher than the published data). Although the metallic radius of Al is not the largest among the modifying elements and the Zr_2Ni_7 phase in ZN-Al is the only one that does not show hypo-stoichiometry among the Zr_2Ni_7 phases observed in this study, Al shows exceptional solubility in Zr_2Ni_7 (the highest among all modifying elements), as seen in Table 4. The

Table 4
Summary of EDS results and assigned phases according to the stoichiometry and XRD results. All composition data are in atomic percentage. Zr_7Ni_{10} (t) and Zr_7Ni_{10}(o) are tetragonal and orthorhombic structures of Zr_7Ni_{10}, respectively.

Alloy	Area	Zr	Ni	X	$(Ni+X)/Zr$	e/a	Phase(s)
ZN-Ni	Fig. 3a-1	41.39	58.61	0.00	1.42	7.52	Zr_8Ni_{21} + ZrNi
	Fig. 3a-2	28.14	71.86	0.00	2.55	8.31	Zr_8Ni_{21}
	Fig. 3a-3	22.77	77.23	0.00	3.39	8.63	Zr_8Ni_{21} + $ZrNi_5$
	Fig. 3a-4	96.23	3.77	0.00	0.04	4.23	ZrO_2
ZN-NiA	Fig. 3b-1	36.51	63.49	0.00	1.74	7.81	Zr_8Ni_{21} + ZrNi
	Fig. 3b-2	30.50	69.50	0.00	2.28	8.17	Zr_8Ni_{21} + ZrNi
	Fig. 3b-3	26.78	73.22	0.00	2.73	8.39	Zr_8Ni_{21}
	Fig. 3b-4	17.52	82.48	0.00	4.71	8.95	$ZrNi_5$
	Fig. 3b-5	96.51	3.49	0.00	0.04	4.21	ZrO_2
ZN-Mg	Fig. 3c-1	37.80	62.20	0.00	1.65	7.73	Zr_7Ni_{10} (t)
	Fig. 3c-2	28.39	70.11	1.50	2.52	8.18	Zr_2Ni_7
	Fig. 3c-3	12.61	24.92	62.47	6.93	4.25	Mg_2Ni
ZN-Al	Fig. 3d-1	36.60	59.20	4.19	1.73	7.51	Zr_7Ni_{10} (t)
	Fig. 3d-2	32.68	59.81	7.51	2.06	7.51	Zr_8Ni_{21} + Zr_7Ni_{10} (t)
	Fig. 3d-3	21.49	66.94	11.57	3.65	7.90	Zr_2Ni_7
	Fig. 3d-4	95.71	3.21	1.08	0.04	4.18	ZrO_2
ZN-AlA	Fig. 3e-1	38.16	58.53	3.31	1.62	7.48	Zr_7Ni_{10} (t)
	Fig. 3e-2	20.75	69.19	10.06	3.82	8.05	Zr_2Ni_7
	Fig. 3e-3	20.62	68.53	10.85	3.85	8.00	Zr_2Ni_7
	Fig. 3e-4	95.46	3.84	0.71	0.05	4.22	ZrO_2
	Fig. 3e-5	92.50	6.38	1.12	0.08	4.37	ZrO_2
	Fig. 3e-6	95.44	3.73	0.83	0.05	4.22	ZrO_2
ZN-Sc	Fig. 3f-1	33.64	61.34	5.02	1.97	7.63	Zr_7Ni_{10} (t)
	Fig. 3f-2	35.56	59.26	5.18	1.81	7.50	Zr_7Ni_{10} (t)
	Fig. 3f-3	25.40	68.17	6.43	2.94	8.03	Zr_2Ni_7
	Fig. 3f-4	10.32	25.70	63.99	8.69	4.90	Sc—Zr solid solution
ZN-ScA	Fig. 3g-1	39.99	56.75	3.26	1.50	7.37	Zr_7Ni_{10} (t)
	Fig. 3g-2	26.01	68.18	5.81	2.84	8.03	Zr_2Ni_7
	Fig. 3g-3	4.76	7.56	87.68	20.01	3.58	Sc—Zr solid solution
ZN-V	Fig. 3h-1	37.16	60.29	2.55	1.69	7.64	Zr_7Ni_{10} (t)
	Fig. 3h-2	29.52	62.83	7.65	2.39	7.85	Zr_2Ni_7
	Fig. 3h-3	23.24	71.40	5.36	3.30	8.34	Phase X
	Fig. 3h-4	93.79	5.70	0.52	0.07	4.35	ZrO_2
ZN-VA	Fig. 3i-1	28.69	64.65	6.67	2.49	7.95	Zr_2Ni_7
	Fig. 3i-2	90.75	8.46	0.79	0.10	4.52	ZrO_2
	Fig. 3i-3	89.63	9.35	1.02	0.12	4.57	ZrO_2
ZN-Mn	Fig. 3j-1	37.00	59.32	3.68	1.70	7.67	Zr_7Ni_{10} (t)
	Fig. 3j-2	22.93	72.27	4.80	3.36	8.48	Phase X
	Fig. 3j-3	26.20	65.94	7.86	2.82	8.19	Zr_2Ni_7
	Fig. 3j-4	93.51	5.94	0.55	0.07	4.37	ZrO_2
ZN-MnA	Fig. 3k-1	39.54	58.53	1.93	1.53	7.57	Zr_7Ni_{10} (t)
	Fig. 3k-2	28.46	64.92	6.63	2.51	8.09	Zr_2Ni_7
	Fig. 3k-3	84.00	14.50	1.50	0.19	4.92	ZrO_2
	Fig. 3k-4	92.76	6.58	0.66	0.08	4.41	ZrO_2
ZN-Co	Fig. 3l-1	40.14	57.92	1.94	1.49	7.57	Zr_7Ni_{10} (t)
	Fig. 3l-2	28.79	63.30	7.91	2.47	8.19	Zr_2Ni_7
	Fig. 3l-3	23.31	68.73	7.97	3.29	8.52	Phase X
	Fig. 3l-4	96.58	3.18	0.24	0.04	4.20	ZrO_2
ZN-CoA	Fig. 3m-1	28.58	64.95	6.47	2.50	8.22	Zr_2Ni_7
	Fig. 3m-2	29.16	64.68	6.17	2.43	8.19	Zr_2Ni_7
	Fig. 3m-3	23.15	71.36	5.50	3.32	8.56	Phase X
	Fig. 3m-4	93.81	5.87	0.31	0.07	4.37	ZrO_2
ZN-Sn	Fig. 3n-1	27.13	48.88	23.99	2.69	9.33	Zr_2Ni_2Sn
	Fig. 3n-2	37.33	60.98	1.69	1.68	7.83	Zr_7Ni_{10} (t)
	Fig. 3n-3	26.40	63.04	10.56	2.79	8.84	$ZrNi_2Sn$
	Fig. 3n-4	28.46	71.09	0.44	2.51	8.31	Zr_2Ni_7
	Fig. 3n-5	24.68	75.54	0.77	3.09	8.65	Phase X
	Fig. 3n-6	89.72	9.38	0.90	0.11	4.65	ZrO_2
ZN-SnA	Fig. 3o-1	40.80	40.69	18.51	1.45	8.29	Zr_2Ni_2Sn
	Fig. 3o-2	27.39	48.00	24.61	2.65	9.34	$ZrNi_2Sn$
	Fig. 3o-3	26.89	48.10	25.01	2.72	9.39	$ZrNi_2Sn$
	Fig. 3o-4	28.71	70.88	0.42	2.48	8.30	Zr_8Ni_{21}
	Fig. 3o-5	29.62	69.62	0.76	2.38	8.25	Zr_8Ni_{21}
	Fig. 3o-6	93.36	5.63	1.01	0.07	4.44	ZrO_2
ZN-La	Fig. 3p-1	0.21	49.51	50.28	475.19	6.47	LaNi
	Fig. 3p-2	40.23	59.33	0.45	1.49	7.56	Zr_7Ni_{10} (o)
	Fig. 3p-3	28.67	71.04	0.29	2.49	8.26	Zr_8Ni_{21}
	Fig. 3p-4	0.26	80.64	19.10	383.62	8.65	$LaNi_5$
ZN-LaA	Fig. 3q-1	0.10	49.67	50.23	999.00	6.48	LaNi
	Fig. 3q-2	4.71	53.71	41.58	20.23	6.81	LaNi
	Fig. 3q-3	42.56	57.27	0.17	1.35	7.43	Zr_7Ni_{10} (o)
	Fig. 3q-4	28.65	71.16	0.19	2.49	8.27	Zr_8Ni_{21}
	Fig. 3q-5	96.15	3.61	0.24	0.04	4.21	ZrO_2
	Fig. 3q-6	0.27	77.66	22.07	369.37	8.44	La_2Ni_7

Table 4 (*Continued*)

Alloy	Area	Zr	Ni	X	$(Ni+X)/Zr$	e/a	Phase(s)
ZN-Hf	Fig. 3r-1	30.55	66.55	2.90	2.27	7.99	$Zr_8Ni_{21}+Zr_7Ni_{10}$ (o)
	Fig. 3r-2	26.93	70.64	2.43	2.71	8.24	$Zr_8Ni_{21}+Zr_7Ni_{10}$ (o)
	Fig. 3r-3	19.66	77.94	2.40	4.09	8.68	Zr_8Ni_{21}
ZN-HfA	Fig. 3s-1	32.02	65.14	2.83	2.12	7.91	$Zr_8Ni_{21}+Zr_7Ni_{10}$ (o)
	Fig. 3s-2	29.46	68.12	2.41	2.39	8.09	$Zr_8Ni_{21}+Zr_7Ni_{10}$ (o)
	Fig. 3s-3	19.62	77.94	2.44	4.10	8.68	Zr_8Ni_{21}
	Fig. 3s-4	22.36	76.16	1.47	3.47	8.57	Zr_8Ni_{21}
	Fig. 3s-5	96.12	0.81	3.08	0.04	4.04	ZrO_2

addition of the larger Al in the B-site is responsible for the Zr_2Ni_7 unit cell enlargement in ZN-Al. The SEM micrograph shows parallel band-structure of the Zr_7Ni_{10}, Zr_2Ni_7, and $Zr_8Ni_{21}+Zr_7Ni_{10}$ phases (Fig. 3c).

After annealing, the major features in the XRD pattern remain unchanged. The abundance of the main phase Zr_7Ni_{10} (t) increases while the minor phases such as ZrNi and Zr_8Ni_{21} decrease (Fig. 2e). The unit cell volumes of both Zr_7Ni_{10} (t) and Zr_2Ni_7 remain the same after annealing due to their similar compositions compared to before annealing. The SEM micrograph shows a different banded pattern where a uniform band and a matrix-intergrowth band alternate throughout the sample (Fig. 3d). In the area covered by this micrograph, the uniform band is Zr_2Ni_7 while the other is Zr_2Ni_7 imbedded in the Zr_7Ni_{10} matrix.

3.4. $Zr_8Ni_{19}Sc_2$ alloy

Sc has an electronegativity and metallic radius similar to those of Mg but has a smaller difference in number of outer-shell electrons when compared to Ni. Additionally, Sc forms a total solid solution with Zr, which is contrary to the case for Mg. Therefore a higher ratio of Sc to Zr than in the case of ZN-Mg is expected in all Zr-containing phases. The XRD pattern of ZN-Sc shows Zr_7Ni_{10} (t) and FCC Zr_2Ni_7 phases (Fig. 2f). The unit cell volume of Zr_7Ni_{10} (t) is similar to that from ZN-Mg and ZN-Al. However, the unit cell volume of Zr_2Ni_7 is between those of ZN-Mg and Zn—Al due to the following phenomena: also affected by the hypo-stoichiometry in Zr_2Ni_7 phase, the solubility of Sc in Zr_2Ni_7 is higher than that of Mg as predicted and evidently seen in the EDS results; moreover, although Sc is larger than Al in size, the solubility of Sc in Zr_2Ni_7 is lower. The SEM micrograph shows a matrix mainly of Zr_7Ni_{10} with Zr_2Ni_7 intergrowth grains. It is possible that the matrix contains one or more finer phases that are beyond the SEM resolution. The Ni-content in Zr_7Ni_{10} phase is higher than that in Zr_7Ni_{10} phase in ZN-Mg due to the incorporation of other Ni-rich phases (for example, $ZrNi_3$ or Zr_2Ni_7). These small crystallites cannot be seen in the XRD pattern due to their broad peak width. There is also a Sc-rich inclusion embedded in the solid (area 4).

After annealing, the phase abundance of Zr_7Ni_{10} (t) increases (Fig. 2g). The lattice constants of both Zr_7Ni_{10} (t) and Zr_2Ni_7 remain the same after annealing. Small and large areas of Zr_2Ni_7 are seen in the SEM micrograph. Therefore, it is likely that the fine grains in the matrix of unannealed ZN-Sc are Zr_2Ni_7 and grow into the small granules in the annealed sample (also, the Zr_2Ni_7 intergrowth grains of the unannealed sample grow into the large Zr_2Ni_7 in the annealed sample). The Sc-rich inclusion becomes even higher in Sc-content after annealing. As a consequence, the Sc-content in Zr_7Ni_{10} reduces after annealing.

3.5. $Zr_8Ni_{19}V_2$ alloy

V is slightly larger and has a lower electronegativity and fewer number of outer-shell electrons than Ni. The XRD pattern of the unannealed alloy shows a Zr_2Ni_7-predominant structure with a small amount of Zr_7Ni_{10} (t) (Fig. 2h). Although still larger than the unit cell listed in the database, the unit cell of Zr_2Ni_7 is slightly smaller than those of ZN-Mg, ZN-Al, and ZN-Sc due to V's smaller size compared to Mg, Al, and Sc. The unit cell of Zr_7Ni_{10} (t) is much smaller than those from ZN-Mg, ZN-Al, and ZN-Sc and may have been caused by the partial replacement of Zr by the smaller-sized V in the A-site. This finding is different from the result found in the study conducted by Young et al. where V was added into pure $(TiZr)_7Ni_{10}$ alloy, and the unit cell expands due to the partial substitution of Ni by V [11]. The SEM micrograph of ZN-V shows a Zr_2Ni_7 matrix with Zr_7Ni_{10} dendritic secondary phase within. There is also a Ni-rich phase shown as a narrow line (area 3) in the micrograph. Although the XRD analysis did not pick up any extra phase, an XRD reflection peak is found at round 38.4° in some samples (see Sections 3.7 and 3.8) with approximately the same EDS $(Ni+X)/Zr$ ratio compared to area 3 of the ZN-V micrograph. Therefore, this composition of the Ni-rich phase will be designated as Phase X in the rest of this report.

After annealing, the XRD pattern is composed of only peaks from the Zr_2Ni_7 phase (Fig. 2i), with a unit cell slightly greater than that from the annealed sample. There is no trace of either Zr_7Ni_{10} or Phase X in the SEM micrograph.

3.6. $Zr_8Ni_{19}Mn_2$ alloy

Mn is similar in size but has a lower electronegativity and fewer number of outer-shell electrons than Ni. Similar to the case of V-substitution, the XRD of ZN-Mn shows a Zr_2Ni_7-predominant structure with a small amount of Zr_7Ni_{10} (t) (Fig. 2j). While the unit cell of Zr_2Ni_7 is larger than that listed in the database due to its hypo-stoichiometry, the unit cell of the Zr_7Ni_{10} (t) phase is smaller due to its hyper-stoichiometry. Area 2 is labeled as Phase X based on its composition although no corresponding XRD peaks are found. Moreover, the micrograph shows the alternating pattern of Zr_7Ni_{10} (t), Phase X, and Zr_2Ni_7.

After annealing, while peaks from the Zr_7Ni_{10} minor phase cannot be detected by the XRD analysis (Fig. 2k), a small area of the Zr_7Ni_{10} minor phase can still be observed in the SEM micrograph. The unit cell volume of the main phase Zr_2Ni_7 increases slightly after annealing as a result of the reduction in $(Ni+X)/Zr$ ratio.

3.7. $Zr_8Ni_{19}Co_2$ alloy

Co is similar to Ni in size as in the case of Mn. Moreover, due to their neighboring positions in the periodic table, the electronegativity of Co is very close to that of Ni, and the number of outer-shell electrons of Co is only slightly fewer than that of Ni. As discussed in the cases of V and Mn partial replacements, the XRD of ZN-Co shows a Zr_2Ni_7-predominant structure with a small amount of Zr_7Ni_{10} (t) (Fig. 2l). In addition, small peaks attributed to $ZrNi_5$ (around 44.8°) and Phase X (around 38.4°) are also observed. Both unit cell volumes of Zr_2Ni_7 and Zr_7Ni_{10} (t) are similar to those from ZN-Mn alloy due to the same deviations from the stoichiometric ratios in ZN-Mn. In the SEM micrograph, area 3 with slightly darker contrast has a high Ni-content and is assigned as Phase X (Fig. 3e). The $ZrNi_5$ phase identified by XRD is not visible in the SEM micrograph. A

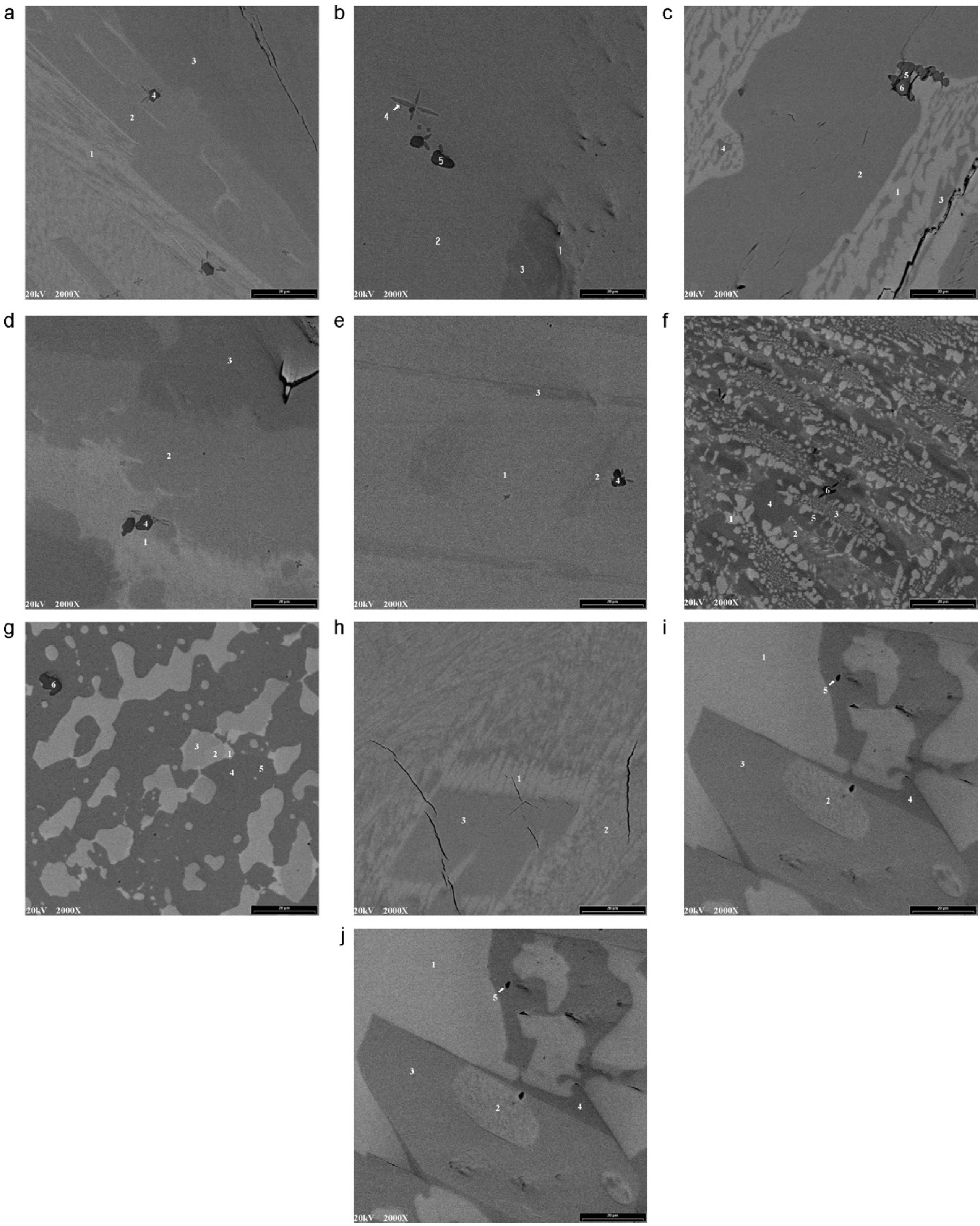

Fig. 3. SEM backscattering images for ZN-Ni (a), ZN-NiA (b), ZN-Al (c), ZN-AlA (d), ZN-Co (e), ZN-CoA (f), ZN-Sn (g), ZN-SnA (h), ZN-Hf (i), and ZN-HfA (j) samples. The chemical compositions of the indexed areas measured by EDS are summarized in Table 4.

more random-shape alternating pattern of Zr_7Ni_{10} (t), Zr_2Ni_7, and Phase X is observed.

After annealing, the XRD peaks from the Zr_7Ni_{10} minor phase disappear, but the peak from Phase X remains (Fig. 2m). The unit cell volume of the main phase Zr_2Ni_7 reduces slightly after annealing. The SEM micrograph exhibits a uniform Zr_2Ni_7 background with occasional streaks of Phase X (Fig. 3f).

Since only Zr_2Ni_7 peaks and the peak at 38.4° are present in the XRD pattern and only Zr_2Ni_7 and a high Ni-content phase are observed in the SEM micrograph, ZN-CoA has directly validated the linking of the peak at 38.4° to an EDS calculated Ni-rich stoichiometry of approximately Zr_2Ni_7, or Phase X. This finding in ZN-CoA is the base of all Phase X designations in the samples discussed earlier. Furthermore, Phase X may be another crystal structure with a nominal Zr_2Ni_7 stoichiometry, which has not been formerly reported.

3.8. $Zr_8Ni_{19}Sn_2$ alloy

Sn has a larger metallic radius than Ni. Also, Sn is the only modifying element used in this study having more outer-shell electrons and a larger electronegativity than Ni. Sn as an additive in AB_2 MH alloy has been studied extensively for the purpose of reducing raw material costs by using zircaloy scrap (Zr—Sn) [28]. The research shows that small amounts of Sn occupy the A-site and replace Zr, while larger amounts of Sn occupy the B-site [28]. The XRD pattern of ZN-Sn shows a Zr_2Ni_7-predominant structure with many secondary phases such as $ZrNi_5$, Phase X, and two Sn-containing $ZrNi_2Sn$ and Zr_2Ni_2Sn (Fig. 2n). The unit cell of the Zr_2Ni_7 phase is larger than that listed in the database due to its hypo-stoichiometry. The SEM micrograph shows a large number of small intergrowths of various secondary phases (mainly $ZrNi_2Sn$) within the matrix of Zr_2Ni_7 (Fig. 3g). The Sn-content in Zr_xNi_y phases are lower due to the formation of Sn-containing phases.

The XRD pattern of ZN-SnA shows a substantial reduction in Zr_2Ni_7 and the appearance of Zr_8Ni_{21} (Fig. 2o). The phase abundance of $ZrNi_2Sn$ increases at the expense of Zr_2Ni_2Sn. In the SEM micrograph, larger inclusions of $ZrNi_2Sn$ and Zr_2Ni_2Sn Sn-rich phases can be observed within the Sn-poor Zr_8Ni_{21} matrix (Fig. 3h). Sn, when combined with annealing, is the only supplemental element that promotes an increase in Zr_8Ni_{21} phase abundance.

3.9. $Zr_8Ni_{19}La_2$ alloy

La is the largest modifying element of the series; however, it has one of the lower numbers of outer-shell electrons and the lowest electronegativity among all the modifying elements. La was selected as a supplement that would potentially enlarge the unit cell and increase the M—H bonding, consequently enhance the storage capacity. The XRD pattern of ZN-La shows two predominant Zr_8Ni_{21} and orthorhombic-structured Zr_7Ni_{10} phases with two La-containing LaNi and $LaNi_5$ phases (Fig. 2p). The unit cell volumes of Zr_7Ni_{10} (o) and Zr_8Ni_{21} are similar to those listed in the database. Additionally, the unit cell of the Zr_8Ni_{21} phase is larger than that of the base alloy ZN-Ni due to the larger-sized La occupying the B-site and its lower (Ni + X)/Zr ratio compared to that in ZN-Ni. The SEM micrograph shows random crisscrossing matrices of larger Zr_8Ni_{21} grains and granular mixtures of the Zr_7Ni_{10} and Zr_8Ni_{21} phases. Occasionally, large inclusions of LaNi and $LaNi_5$ mixtures are found due to the immiscibility between La and Zr. Only very small amounts of La are present in Zr_xNi_y phases.

After annealing, the phase abundance of Zr_7Ni_{10} (o) increases and a new Zr_2Ni_7 phase appears at the expense of Zr_8Ni_{21} (Fig. 2q). Due to the hypo-stoichiometry in the Zr_2Ni_7 phase, its unit cell is larger than that listed in the database. According to the EDS results, the unit cell of Zr_7Ni_{10} (o) is smaller than that from the unannealed sample as a result of the reduction in La. In the SEM micrograph, the main phase Zr_7Ni_{10} and La-containing phases have grown into larger grains after annealing. Also, after annealing, each phase becomes more distinct. It should be noted that the stoichiometries in Zr_7Ni_{10} (o) and Zr_8Ni_{21} phases are very close to the ideal ratio.

3.10. $Zr_8Ni_{19}Hf_2$ alloy

Hf is the only substituting element in the same group as Zr. Along with Zr and Ti, Hf is one of the commonly used A-site elements for AB_2 alloys. Ti was not chosen due to its smaller size and its modifying effect of increasing the already higher hydride heat of formation of Zr_8Ni_{21} [36]. Other than its slightly smaller metallic radius, Hf has very similar chemical properties to Zr and forms a solid solution with Zr during solidification. Therefore, Hf is expected to occupy the A-site and partially replaces Zr. The XRD pattern of ZN-Hf shows a combination of Zr_8Ni_{21} and Zr_7Ni_{10} (o) (Fig. 2r). No new Hf-containing phase is found as in the cases of other large atom-substitutions, such as Mg, Sc, Sn, and La. The unit cells of Zr_7Ni_{10} (o) and Zr_8Ni_{21} are smaller than those listed in the database. In fact, the unit cell of Zr_8Ni_{21} is the smallest among all Zr_8Ni_{21} phases observed in this study. Since Hf is likely in the A-site, its smaller size compared to Zr reduces the unit cell volumes of Zr_7Ni_{10} (o) and Zr_8Ni_{21}. The SEM micrograph shows an uneven distribution of small Zr_7Ni_{10} grains in the matrix of Zr_8Ni_{21} phase (Fig. 3i). Occasionally, large grains of Zr_8Ni_{21} are apparent (area 3). In other areas, Zr_7Ni_{10} is mixed in with Zr_8Ni_{21} at difference ratios. The assigned Zr_8Ni_{21} phase has a (Ni + X)/Zr ratio that is higher than the stoichiometry of Zr_8Ni_{21} due to the possible occupancy of Hf in the A-site.

After annealing, there is no major change in the XRD pattern (Fig. 2s). While the unit cell volume of Zr_8Ni_{21} remains the same, the unit cell of Zr_7Ni_{10} (o) is smaller than that of the unannealed sample. According to the SEM micrograph of ZN-HfA, the sizes of

Table 5
Summary of XRD and EDS results.

	Main phase	Phase distribution
ZN-Ni	Zr_8Ni_{21} (triclinic)	Zr_8Ni_{21} matrix with very fine ZrNi grains
ZN-NiA	Zr_8Ni_{21} (triclinic)	Zr_8Ni_{21} matrix with very fine ZrNi grains
ZN-Mg	Zr_7Ni_{10} (tetragonal)	Zr_7Ni_{10} matrix with Zr_2Ni_7 grains
ZN-Al	Zr_7Ni_{10} (tetragonal)	Zr_7Ni_{10}—Zr_2Ni_7—(Zr_8Ni_{21} + Zr_7Ni_{10}) banded pattern
ZN-AlA	Zr_7Ni_{10} (tetragonal)	Zr_7Ni_{10}—Zr_2Ni_7 banded pattern
ZN-Sc	Zr_7Ni_{10} (tetragonal)	Zr_7Ni_{10} matrix with Zr_2Ni_7 grains
ZN-ScA	Zr_7Ni_{10} (tetragonal)	Zr_7Ni_{10} matrix with Zr_2Ni_7 grains
ZN-V	Zr_2Ni_7 (cubic)	Zr_2Ni_7 with Zr_7Ni_{10} secondary phase
ZN-VA	Zr_2Ni_7 (cubic)	Zr_2Ni_7 only
ZN-Mn	Zr_2Ni_7 (cubic)	Zr_2Ni_7—Zr_7Ni_{10} banded pattern
ZN-MnA	Zr_2Ni_7 (cubic)	Zr_2Ni_7 with Zr_7Ni_{10} secondary phase
ZN-Co	Zr_2Ni_7 (cubic)	Zr_2Ni_7 with Zr_7Ni_{10} secondary phase
ZN-CoA	Zr_2Ni_7 (cubic)	Zr_2Ni_7 only
ZN-Sn	Zr_2Ni_7 (cubic)	Zr_2Ni_7 matrix with Zr_7Ni_{10} and Sn-rich grains
ZN-SnA	Zr_8Ni_{21} (triclinic)	Zr_8Ni_{21} matrix with Sn-rich grains (ZN-SnA)
ZN-La	Zr_7Ni_{10} (orthorhombic)	Zr_7Ni_{10} matrix with Zr_8Ni_{21} secondary phase and La-rich grains
ZN-LaA	Zr_7Ni_{10} (orthorhombic)	Zr_7Ni_{10} matrix with Zr_8Ni_{21} secondary phase and La-rich grains
ZN-Hf	Zr_7Ni_{10} (orthorhombic)	Zr_7Ni_{10} matrix with Zr_8Ni_{21} secondary phase
Zn-HfA	Zr_7Ni_{10} (orthorhombic)	Zr_7Ni_{10} matrix with Zr_8Ni_{21} secondary phase

grains are greater after annealing (Fig. 3j). Areas 1 and 2 are from the mixtures of Zr_7Ni_{10} and Zr_8Ni_{21} determined by the compositions, and areas 3 and 4 are Zr_8Ni_{21} with different compositions. Since both Zr_8Ni_{21} and Hf_8Ni_{21} phases are stable inter-metallic alloys, the $(ZrHf)_8Ni_{21}$ alloy should exist over a large range of Zr/Hf composition. Moreover, not all A-sites are equivalent [15]; therefore, there may be some preferential A-sites for the Hf atom in the A_8B_{21} structure, which accounts for the two phases that have the same structure but slightly different compositions (area 3 and 4).

4. Summary

The effects of partial-Ni substitution and annealing treatment on the structural properties of Zr_8Ni_{21}, a candidate to replace the currently used misch-metal based AB_5 MH alloy, have been presented. With the exception of Sn-substitution, the general effect of annealing is an increase in abundance of the predominant phase and reductions in both number and abundance of secondary phases. The major phase of the Sn-containing alloy transforms from Zr_2Ni_7 to Zr_8Ni_{21}. Summarized in Table 5, the microstructures of materials in this study can be classified into four groups according to their main phase: Zr_8Ni_{21}, Zr_7Ni_{10} (t), Zr_2Ni_7, and Zr_7Ni_{10} (o).

By comparing this summary to the properties of the supplement elements as listed in Table 1, it can be seen that the number of outer-shell electrons has a direct correlation with the choice of the main phase. As the number of outer-shell electrons, which determines the average electron density (e/a), increases in the order of $(Mg < Sc = Al) = (La < Hf) < (V < Mn < Co) < (Ni < Sn)$, the main phase of the annealed samples evolves from Zr_7Ni_{10} (t), to Zr_7Ni_{10} (o), Zr_2Ni_7, and finally Zr_8Ni_{21}. The same parameter also controls the choice between the two main structures for AB_2 alloys [37–43], where, as e/a increases, the structure transforms from hexagonal C14 to FCC C15. As the B-content in main phase increases, the maximum and reversible hydrogen storage capacities are expected to decrease and increase, respectively.

Acknowledgements

The financial supports from Michigan Initiative for Innovation & Entrepreneurship (2009) and the Department of Energy (Grant DE-EE0002106) for this research are gratefully acknowledged.

References

[1] M.A. Fetcenko, S.R. Ovshinsky, B. Reichman, K. Young, C. Fierro, J. Koch, A. Zallen, W. Mays, T. Ouchi, J. Power Sources 165 (2007) 544.
[2] News article available online: http://www.technewsdaily.com/us-congress-pushes-independence-from-chinese-rare-earth-suppliers-0325/.
[3] S.R. Ovshinsky, M.A. Fetcenko, J. Ross, Science 260 (1993) 176.
[4] J.M. Joubert, M. Latroche, A. Percheron-Guégan, J. Alloys Compd. 231 (1995) 494.
[5] J.M. Joubert, M. Latroche, A. Percheron-Guégan, J. Bouet, J. Alloys Compd. 240 (1996) 219.
[6] H. Nakano, S. Wakao, T. Shimizu, K. Morii, J. Electrochem. Soc. Jpn. 66 (1998) 734.
[7] K. Hong, J. Alloys Compd. 321 (2001) 307.
[8] H. Okamoto, J. Phase Equilib. Diffus. 28 (2007) 409.
[9] T.B. Massalski, Binary Alloy Phase Diagrams, 2nd ed., ASM International, OH, USA, 1990.
[10] K. Young, T. Ouchi, Y. Liu, B. Reichman, W. Mays, M.A. Fetcenko, J. Alloys Compd. 480 (2009) 521.
[11] K. Young, T. Ouchi, M.A. Fetcenko, W. Mays, B. Reichman, Int. J. Hydrogen Energy 34 (2009) 8695.
[12] K. Young, T. Ouchi, B. Huang, J. Nei, M.A. Fetcenko, J. Alloys Compd. 501 (2010) 236.
[13] K. Young, J. Nei, B. Huang, T. Ouchi, M.A. Fetcenko, J. Alloys Compd. 501 (2010) 245.
[14] L. Bsenko, J. Less-Common Met. 63 (1979) 171.
[15] J.M. Joubert, R. Cerný, K. Yvon, Z. Kristallogr, New Cryst. Struct. 213 (1998) 227.
[16] L. Bsenko, Acta Crystallogr., Sect. B: Struct. Sci. 34 (1978) 3204.
[17] F.C. Ruiz, E.B. Castro, H.A. Peretti, A. Visintin, Int. J. Hydrogen Energy 35 (2010) 9879.
[18] H. Pan, J. Ma, C. Wang, S. Chen, X. Wang, C. Chen, Q. Wang, J. Alloys Compd. 293–295 (1999) 648.
[19] B. Liao, Y.Q. Lei, L.X. Chen, G.L. Lu, H.G. Pan, Q.D. Wang, J. Alloys Compd. 376 (2004) 186.
[20] R. Li, H. Pan, M. Gao, H. Miao, Y. Lei, J. Alloys Compd. 432 (2007) 183.
[21] Y. Liu, H. Pan, M. Gao, H. Miao, Y. Lei, Q. Wang, Int. J. Hydrogen Energy 33 (2008) 124.
[22] H. Miao, M. Gao, Y. Liu, D. Zhu, H. Pan, J. Power Sources 184 (2008) 627.
[23] K. Young, T. Ouchi, J. Koch, M.A. Fetcenko, J. Alloys Compd. 477 (2009) 749.
[24] K. Young, T. Ouchi, B. Reichman, W. Mays, R. Regmi, G. Lawes, M.A. Fetcenko, A. Wu, J. Alloys Compd. 489 (2010) 202.
[25] K. Young, R. Regmi, G. Lawes, T. Ouchi, B. Reichman, M.A. Fetcenko, A. Wu, J. Alloys Compd. 490 (2010) 282.
[26] Y. Zhao, M. Gao, Y. Liu, L. Huang, H. Pan, J. Alloys Compd. 496 (2010) 454.
[27] Y. Liu, Y. Cao, L. Huang, M. Gao, H. Pan, J. Alloys Compd. 509 (2011) 675.
[28] K. Young, M.A. Fetcenko, T. Ouchi, F. Li, J. Koch, J. Alloys Compd. 469 (2009) 406.
[29] Y. Zhu, H. Pan, Y. Liu, R. Li, Q. Jin, Q. Wang, Chin. J. Nonferr. Met. 13 (2003) 680.
[30] K. Young, M.A. Fetcenko, F. Li, T. Ouchi, J. Koch, J. Alloys Compd. 468 (2009) 482.
[31] Powder Diffraction File Database Published by International Center for Diffraction Data, Newtown Square, Pennsylvania, 2010.
[32] K. Young, J. Nei, T. Ouchi, M.A. Fetcenko, J. Alloys Compd. 509 (2011) 2277.
[33] L. Bendersky, K. Wang, W. Boettinger, D. Newbury, K. Young, B. Chao, Metall. Mater. Trans. A 41 (2010) 1891.
[34] H.T. Takeshita, N. Fujiwara, T. Oishi, D. Noréus, N. Takeichi, N. Kuriyama, J. Alloys Compd. 360 (2003) 250.
[35] H.T. Takeshita, S. Kondo, H. Miyamura, N. Takeichi, N. Kuriyama, T. Oishi, J. Alloys Compd. 376 (2004) 268.
[36] K. Young, M.A. Fetcenko, F. Li, T. Ouchi, J. Alloys Compd. 464 (2008) 238.
[37] D. Shaltiel, I. Jacob, D. Davidov, J. Less-Common Met. 53 (1977) 117.
[38] J.H. Zhu, P.K. Liaw, C.T. Liu, Mater. Sci. Eng., A 239–240 (1997) 260.
[39] J.H. Zhu, C.T. Liu, P.K. Liaw, Intermetallics 7 (1999) 1011.
[40] B. Chao, R.C. Young, S.R. Ovshinsky, D.A. Pawlik, B. Huang, J.S. Im, B.C. Chakoumakos, in: D. Doughty, L. Nazar, M. Arakawa, H.-P. Brack, K. Naoi (Eds.), New Materials for Batteries and Fuel Cells, Materials Research Society Symposium, Materials Research Society, San Francisco, California, USA, 1999, p. 193.
[41] Z. Shi, S. Chumbley, F.C. Laabs, J. Alloys Compd. 312 (2000) 41.
[42] S. Amerioun, T. Yokosawa, S. Lidin, U. Häussermann, Inorg. Chem. 43 (2004) 4751.
[43] K. Young, T. Ouchi, B. Huang, B. Chao, M.A. Fetcenko, L.A. Bendersky, K. Wang, C. Chiu, J. Alloys Compd. 506 (2010) 841.
[44] A.L. Allred, J. Inorg. Nucl. Chem. 17 (1961) 215.
[45] C. Kittel, Introduction to Solid State Physics, 7th ed., John Wiley & Sons, New York, 1990.
[46] D.R. Lide, CRC Handbook of Chemistry and Physics, 74th ed., CRC Press, Ann Arbor, 1994.